12th International Symposium on Turbulence and Shear Flow Phenomena (TSFP12)
Osaka, Japan (Online), July 19-22, 2022

THREE-DIMENSIONAL TURBULENT JET STUDY USING VOLUMETRIC PARTICLE TRACKING VELOCIMETRY

Nimesh Virani
Department of Mechanical, Automotive and Materials Engineering
University of Windsor
401 Sunset Avenue, Windsor, Ontario, N9B 3P4, Canada
viranin@uwindsor.ca

Vesselina Roussinova
Department of Mechanical, Automotive and Materials Engineering
University of Windsor
401 Sunset Avenue, Windsor, Ontario, N9B 3P4, Canada
vtr@uwindsor.ca

Ram Balachandar
Department of Civil and Environmental Engineering
University of Windsor
401 Sunset Avenue, Windsor, Ontario, N9B 3P4, Canada
rambala@uwindsor.ca

ABSTRACT

This paper presents the three-dimensional (3D) evaluation of a turbulent free jet using volumetric particle tracking velocimetry (3D-PTV). The volumetric measurements (V3V^{TM}) results are complemented with laser Doppler velocimetry (LDV) measurements. Mean velocity and turbulence quantities calculated from both techniques are compared, and similarities, as well as differences in results, are discussed. Special attention is paid to achieving higher spatial resolution in the depth-wise direction for the volumetric measurements. A final resolution of 0.036d is achieved, (where d is the jet exit diameter) in the depth-wise direction. Measurement uncertainty estimates are calculated for the V3V measurements based on a systematic approach to quantify the uncertainty based on the volumetric calibration and reconstruction error. The turbulent jet has a Reynolds number of 38,500 based on the nozzle exit diameter (d) of 7 mm and exit velocity, U_j, of 5.5 m/s. Due to V3V's capability of providing access to all nine components of the velocity gradient tensor, the study of jet's behaviour in the spanwise plane is feasible. Global jet entrainment at different axial positions is calculated for the spanwise plane and compared with the results in literature.

INTRODUCTION

The evaluation of large-scale coherent structures in the near-field of a turbulent jet requires the complete velocity field (i.e. three velocity components) in the 3D domain (Liepmann and Gharib, 1992; Discetti and Coletti, 2018). Such full volumetric (3D-3C, i.e., three-dimensional and three-components) measurements become possible with the advent of new hardware in photogrammetry and advanced processing algorithms. Several studies explored the near field dynamics of the coherent structures and their effects on the self-similar zone of a turbulent axisymmetric jet, starting from the seminal work of Crow and Champagne (1971) and George (1988) among others. Recently, the tomographic particle image velocimetry (Tomo-PIV) technique was used by Breda and Buxton (2019) to obtain 3D velocity measurements. The study investigated the effect of coherent structures in the near field of a turbulent jet and their effect on the rate of entrainment. Similar, investigations by Violato and Scarano (2011, 2013) attempted to understand the 3D behaviour of flow transition and jet core breakdown in circular jets, which plays a considerable role in the generation of acoustic noise.

The measurement performance of Tomo-PIV relies on a high concentration of successfully reconstructed particles in the measurement volume. Higher seeding particles in the flow can boost the number of reconstructed particles after the processing stage, albeit, it results in the ambiguity of the reconstruction process and ghost particles (Elsinga et al., 2011; Discetti and Coletti, 2018). To overcome this limitation, Boomsma and Troolin (2018) implemented a novel technique for particle reconstruction with improved accuracy and reconstruction density called Dense Particle Identification and Reconstruction (DPIR). It can manage particle image density of 0.05 ppp with a reconstruction rate of 91 % real particles. Owing to DPIR's superior performance in the reconstruction of particles and volumetric PTV's capability of achieving fine measurement resolution, we have performed volumetric PTV with the DPIR algorithm.

The objective of this study is twofold. Performing volumetric measurements provides us with an opportunity to study the jet in the relatively less explored spanwise plane, and we have also complemented the analysis with the well-established LDV technique. LDV dataset facilitates the validation of the more recently introduced volumetric technique. Additionally, LDV measurements are time-resolved, and they can capture contributions from small-scale flow structures, hence, using it as a reference confirms V3V's ability to capture small-scale turbulence.

Experiments were performed in the jet experimental facility at the University of Windsor. The jet is generated from a pipe, with a diameter d = 7 mm and 70 mm long. It is released into a quiescent water channel filled with water and with a cross-section of 43d wide and 43d deep. In the streamwise direction, the channel is 200d long. The jet opening is at the centre of the channel in the spanwise and depth-wise directions. The water channel is made from a transparent plexiglass material, which enabled optical access for velocity measurement. For this study, x, y, and z coordinates refer to streamwise, transverse and spanwise directions, respectively. The instantaneous velocity

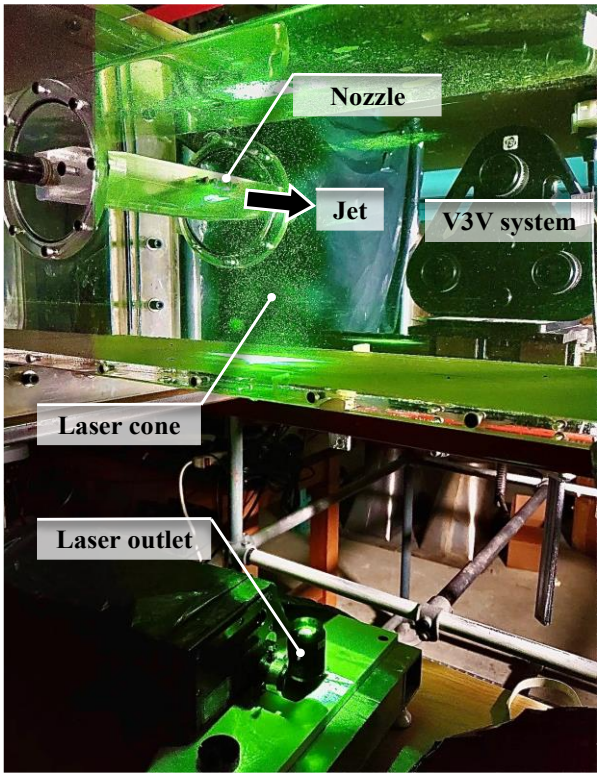

Figure 1. Experimental setup and V3V measurement system arrangement

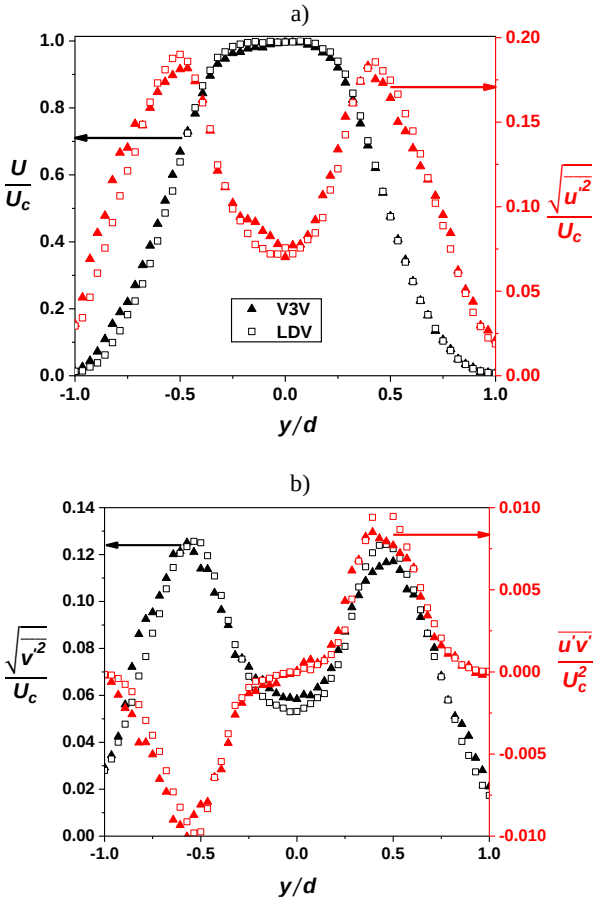

Figure 2. Comparison between LDV and V3V results in the radial direction at a streamwise location of $x = 3d$

and corresponding velocity fluctuations are denoted by u, v, w, and u', v', and w', respectively. The associated mean velocities are defined by U, V, and W. The jet is fed by an overhead water tank which is maintained at a constant level by a continuous water supply from a reservoir using a pump. The jet facility and the experimental setup are shown in Fig. 1.

The commercial V3V system (TSI, Inc.) consists of three PowerView cameras mounted on a custom-designed triangular-shaped stand. A dual pulsed Nd: YAG laser (200 mJ/pulse) and a LaserPulse synchronizer form the essential components of the system. The flow is illuminated by a laser cone generated from 25 mm and 50 mm cylindrical lenses staggered at the laser opening. The flow is seeded with 60 µm polyamide particles. All three cameras have a CCD array with 8 million pixels and 3320 × 2496 resolution, and they are equipped with 50 mm lenses with the aperture setting of f#8. The camera mounting frame is levelled and adjusted to ensure that it is parallel with the channel walls using an alignment laser. Laser pulses are straddled at 100 µs and the measurement was performed at 5 Hz. A total of 1500 images were captured and analyzed with a final measurement volume of $18d \times 13d \times 5d$ in the x, y, and z directions.

Instantaneous vectors are derived from particle images captured using TSI INSIGHTV3V-4G software. A DPIR algorithm based on the work of Boomsma and Troolin (2018) is used in a multi-pass mode for identifying, reconstructing and tracking particles. It starts with the identification of 2D particle locations on camera sensors (in both frames) for all three apertures, which leads to the determination of 3D particle locations in a real-world coordinate system by triangulating each particle using its image from all camera sensors. Once the 3D location is known, particles are tracked between two frames and three velocity components are calculated. Finally, the randomly distributed vectors from all 1500 images are ensembled and statistics are calculated on a regular grid using an in-house MATLAB code. Detailed uncertainty analysis was conducted to quantify the uncertainty levels in all three components of velocity. The w-velocity has a maximum uncertainty of 7% and the other two have less than 3%.

V3V results are complimented with point-wise velocity measurement using a two-velocity component LDV system (Dantec Dynamics Inc.). Two orthogonal velocity components u and v are acquired simultaneously by operating the LDV system in coincidence mode. Laser wavelengths of 532 nm and 561 nm are used for measuring streamwise and transverse velocity components, respectively. To avoid directional ambiguity, a frequency shift is applied by operating a Bragg cell at 80 MHz. The resultant measurement probe volume is 0.194×0.194×3.2 mm^3 with a fringe spacing of 4.55 µm. For signal processing, a BSA F600 processor is used, and data acquisition is controlled by BSA flow software v6.72. Maximum uncertainty for the LDV measurement is less than 3% for turbulence quantities and less than 1% for mean velocities based on a confidence interval of 95%.

RESULTS

For volumetric PTV, mean and turbulence quantities are calculated on a regular grid (equally spaced) by spatial binning and ensemble averaging over 1500 data sets. Here, each snapshot

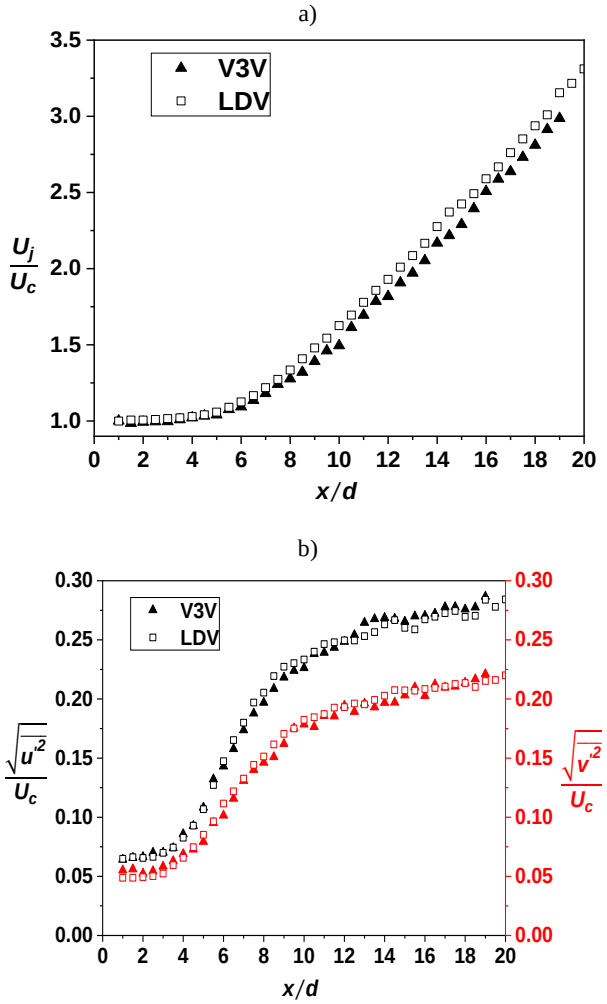

Figure 3. LDV and V3V data along the centerline of the jet

is uncorrelated to each other and vectors for each snapshot are stochastically distributed owing to the Lagrangian approach used for the current case (Godbersen and Schröder, 2020). Unlike PIV, where bin size is restricted by the predefined correlation windows, for the PTV, the bin size is only restricted by the number of available snapshots for ensembling. The process starts by combining randomly spaced 3D vectors in different bins based on their locations. Outlier vectors are first removed by applying a threshold of minimum and maximum absolute velocities for all velocity components. After that standard deviation for each bin is calculated using all available vectors in each bin. Any vectors exceeding the local mean value $\pm 3\sigma$ for u, and v and $\pm 2\sigma$ for w velocity components are removed. Here, σ is the local standard deviation of vectors. Corrected vectors are used for calculating statistics in each bin. Based on the available snapshots and the requirement for maintaining a lower uncertainty level, a final bin size of $2\times1\times1$ mm^3 is achieved with an overlapping of 75 %, which resulted in the final resolution of $0.5\times0.25\times0.25$ mm^3 for the uniform grid. This resolution is equivalent to having 28 measurement points across the diameter of the jet in the radial direction. For consistency, LDV measurement is also performed with the same spatial resolution.

Validation

V3V and LDV measurements are compared near the jet exit at a streamwise location of $x = 3d$. In Fig. 2(a) streamwise mean velocity (on the left axis) and rms of turbulence fluctuations (on the right axis) are compared with the corresponding LDV measurements at the same location. Both quantities are normalized by the local centreline velocity, U_c. Peak turbulence level and mean velocity profile in the potential core and shear layer regions show excellent agreement between the two techniques. In Fig. 2(b), radial profiles of rms of turbulence fluctuations in the transverse direction (y) and Reynolds shear stress are provided. For both Reynolds normal and shear stresses, peak values occur at $y/d = 0.5$, which represents the strong shear in the near field mixing layer of the jet. The linear region of the shear stress profiles near the centre of the jet (at approximately $-0.14< y/d <0.14$), coincides with the linear distribution of shear stress observed for the pipe jet, as reported by (Xu and Antonia, 2002). The near-field radial profiles provide insights into the condition of the jet at the exit of the pipe. Overall, this comparison reiterates that the V3V technique can capture the turbulent statistics faithfully.

The mean streamwise centreline velocity decay is shown in Fig. 3(a) for the data recorded by both techniques. The self-preserving round jet decay rate, K, can be calculated by

$$\frac{U_j}{U_c} = \frac{1}{K}\left(\frac{x}{d} - \frac{x_0}{d}\right) \quad (1)$$

In Eq. (1), x_0 is the virtual origin of the jet. Fitting Eq. (1) to the velocity decay rate data between $x = 10d$ and $x = 20d$ provides the decay rate for LDV and V3V data as 5.97 and 6.12, respectively. These values are similar to what was reported by Boersma et al. (1998) and in reasonable agreement with each other. Apart from the decay rate, the length of the potential core of jet can be estimated by centerline velocity decay data. In the potential core, jet velocity remains almost the same as jet exit velocity, U_j. By fitting a straight line to the velocity decay profile, we found the length of the potential core as $x \approx 5d$.

In Fig. 3(b) rms values of axial and transverse velocity fluctuations normalized by the local centerline velocity are plotted along the centerline of the jet. In the entire potential core region, turbulence levels are constant, and both values linearly increase after the end of the potential core region until $x \approx 10d$. After $10d$, it starts to achieve a plateau region where it remains almost constant at about 25% and 20% levels for streamwise and transverse velocities, respectively. Fig. 3(b) highlights the anisotropic behaviour of turbulence along the centerline of the jet. Where jet anisotropy can be estimated by the ratio between rms values of u-component and v-component of velocity. The maximum anisotropy is found at the immediate region after the end of the potential core, where u' is 35% to 40% more than the v' and/or w', for both cases. Thorough validation of V3V data with LDV in the radial direction as well as along the centerline of the jet using mean quantities and second-order turbulent moments, confirms the suitability of volumetric measurements for further investigation.

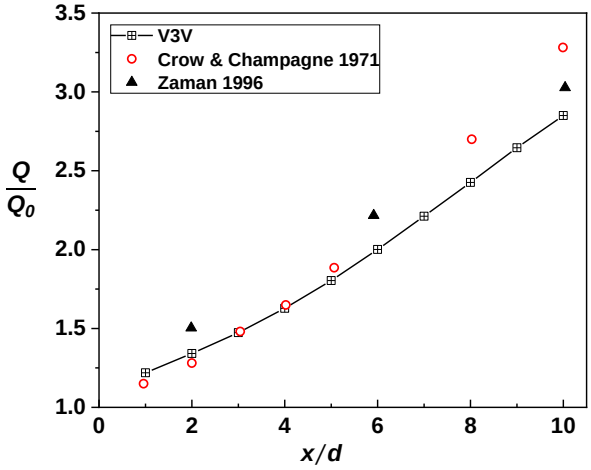

Figure 4. Global entrainment ratio of the jet

Global Jet Entrainment

A full volumetric 3D dataset of jet provides access to the spanwise plane of the jet at different axial locations. This allows studying one of the most interesting properties of the jet, entrainment. Jet entrainment can be calculated using the mean flow data. Usually, it is evaluated based on the streamwise volumetric flow rate Q, which is normalized by its initial value at the nozzle exit, Q_0 (Grinstein, 2001). Here, the volume flux is defined by an area integral over the streamwise mean velocity component following (Wygnanski and Fiedler, 1969; Crow and Champagne, 1971; Liepmann and Gharib, 1992).

$$Q = \int_0^{2\pi} \int_0^{\infty} Ur \, \mathrm{d}r\mathrm{d}\theta \tag{2}$$

Here, r is the radial distance. The initial volumetric flux rate is calculated as $Q_0 = \pi d^2 U_0/4$. The volume flux rate can be calculated at any x location if the radial integration Ur converges. The radial integration can be converged by including enough area in the spanwise plane so that the entire surrounding fluid region affected by the jet is included.

The ratio Q/Q_0 is plotted against the axial distance x/d in Fig. 4. Entrainment calculation is only presented up to x/d = 10 because of the limit on measurement data available in the depth-wise (z) direction. Entrainment calculated from present data shows a good agreement with Crow and Champagne (1971) in the near field until the end of the potential core. Further downstream Q/Q_0 starts deviating from the previous data. This difference can be attributed to the unconverged radial direction integral and/or differences in the initial conditions and experimental facility between Crow and Champagne (1971) and the current case. For comparison rectangular nozzle jet data from Zaman (1996) is also provided in Fig. 4.

Proper Orthogonal Decomposition

To understand the dynamics of large-scale structures and how they are organized in the cross-stream plane, the snapshot implementation of the proper orthogonal decomposition (POD) method is carried out (Sirovich, 1987). POD is a powerful tool that decomposes the flow field based on energy-containing largescale (coherent) structures. It provides a complete orthogonal set of spatial eigenfunctions, which are also known as modes, and ranks the modes based on their energy level. The eigenvalues, λ_i, related to these modes, represent the amount of kinetic energy of the flow field. This essentially means that the low-order modes represent the large-scale structures and higher-order modes correspond to small-scale structures. Here, POD is applied on a spanwise 2D plane (yz) located at the axial location of $x = 3d$. All 1500 snapshots are used for this analysis as they are uncorrelated.

The POD is performed on the fluctuating velocity $\boldsymbol{u}' = [u', v', w']$ of the instantaneous velocity field $\boldsymbol{u} = [u, v, w]$ which can be written as a snapshot matrix $\boldsymbol{U} \in R^{N_t \times p}$. Here, N_t represents the number of snapshots and p is the number of grid points on the 2D plane considered here. Following Essel et al. (2020) and Cortina-Fernández et al. (2021) singular value decomposition (SVD) technique is applied to obtain the decomposition basis in space, $\boldsymbol{\varphi}$, and time, $\boldsymbol{\psi}$ and it decomposes the matrix $\boldsymbol{U}$ as follows

$$\boldsymbol{U} = \boldsymbol{\psi} \sum \boldsymbol{\varphi} \tag{3}$$

where $\boldsymbol{\psi}$ is $N_t \times N_t$ orthogonal matrix, $\boldsymbol{\varphi}$ is $p \times p$ orthogonal matrix and $\sum$ is a non-negative diagonal matrix with the same dimensions as $\boldsymbol{U}$. The matrix $\sum$ contains eigenvalues which represent the energy associated with each mode and is arranged in descending order. Further details about POD method implementation can be found in Sen et al. (2007) and Meyer et al. (2007).

Here, spatial modes φ for all three velocity components (φ_u, φ_v, φ_w) are reconstructed using the low-order modes for understanding the dynamics of energetic structures. These energetic large-scale structures and their effect on jet entrainment were also studied by El Hassan and Meslem (2010) for orifice jets. POD is a tool which facilitates the separation of these structures from the overall flow and hence it is applied in the present study for a circular pipe jet case. The first 10 modes are reconstructed and some of the selected ones are used in Fig. 5 to discuss the flow field. The vectors are plotted using the in-plane components (φ_v, φ_w) and iso-contours represent the out-of-plane (φ_u) component. In this way contribution from all three velocity components is included. The contours in Fig. 5 reveal high ($\varphi_u > 0$) and low ($\varphi_u < 0$) momentum regions (Essel et al., 2020) and it is normalized by the maximum value of φ_u among all the modes presented here. The red circle indicates the approximate edge of the jet for all the modes. The jet edge is identified by a line on which, mean streamwise velocity of the jet becomes 10% of the local centerline velocity at $x = 3d$.

The first mode has kidney-shaped distinct high and low momentum regions. This confirms the presence of large-scale structures and their role in the entrainment of the jet, which is highlighted by drawing the in-plane streamtraces. Streamtraces demonstrate the entrainment mechanism by two distinct regions of the jet, one is a circular region approximately at the edge of the jet and another is at the center of the jet where all streamtraces converge. The second mode contains the ring shape structure with low momentum and the related entrainment process is revealed by the in-plane vectors. The jet edge circle covers the entire zone where entrainment occurs.

In Fig. 5, odd and even number modes are divided between the left and right columns. For brevity, some of the modes are

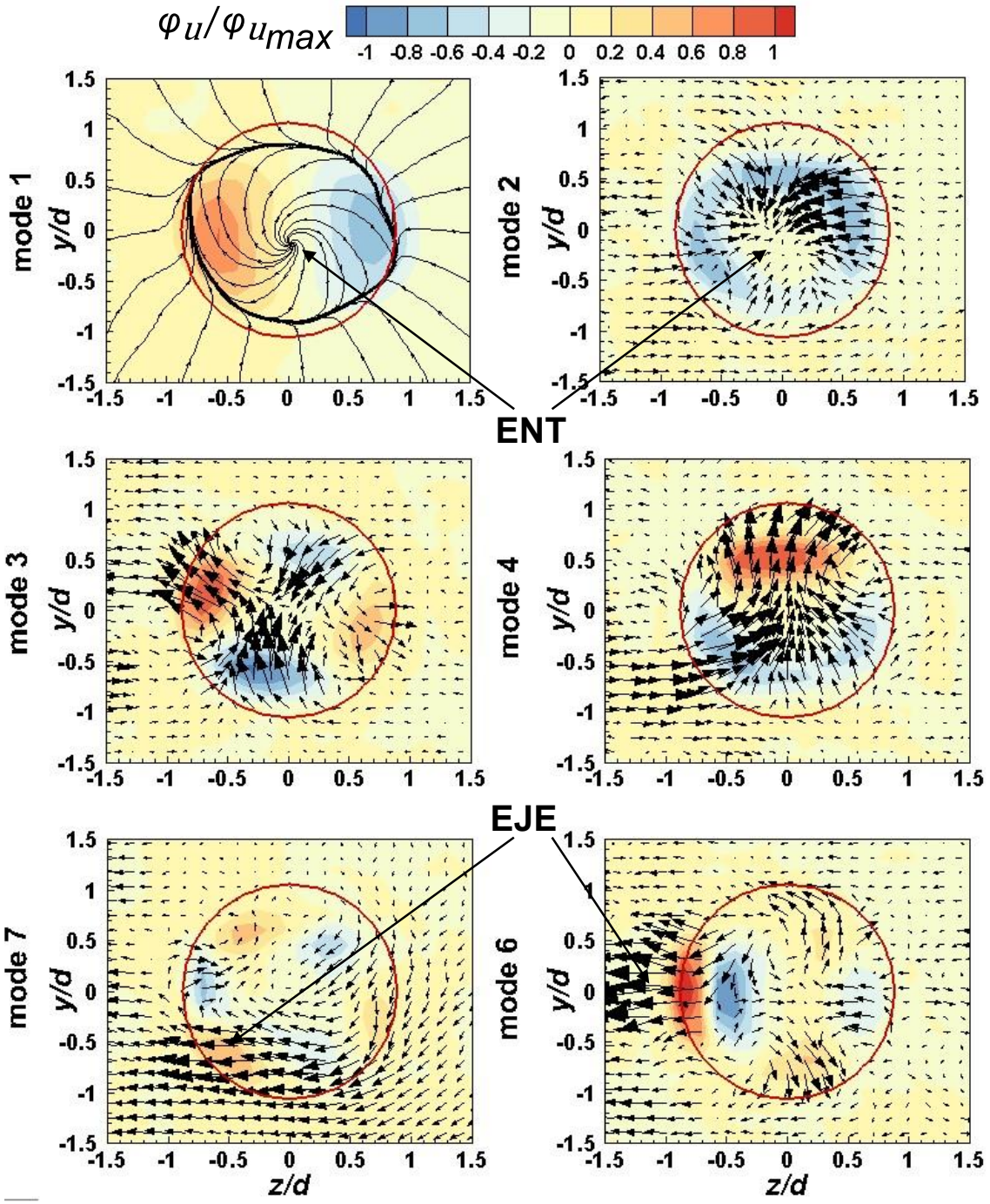

Figure 5. Iso-contours of φ_u of POD modes 1, 2, 3, 4, 6, and 7 with superimposed vectors generated by φ_v and φ_w for the spanwise plane at $x = 3d$. The red circle shows the approximate edge of jet at the given axial location based on 10% of streamwise mean velocity. Here, ENT and EJE represent entrainment and ejection, respectively.

skipped and only the one which shows distinct spatial structures are presented. As the mode number increases, the organization of structures change for both odd and even number modes, albeit in a unique way. However, one thing remains common for all the modes is that entrainment and ejection both occur within the area covered by the jet edge. Previous researchers Liepmann and Gharib (1992) and Romano (2002) discussed the role of ejection of secondary transverse fluid and their relation to Kelvin-Helmholtz shear layer primary instabilities in axisymmetric jets. This ejection of fluid can be related to a secondary counter-rotating mushroom shape structure found in the spanwise plane. Traces of similar kinds of structures can be observed in higher-order modes (3, 4 and 7) in Fig. 5. These structures are very similar to the counter-rotating vortices reported by Capone et al. (2013) in the cross-stream plane at $x = 2.5d$. Although, they reported these vortices using velocity vectors from flow snapshots captured with a high-speed acquisition method, their resemblance to the present structures is remarkable.

CONCLUSION

Volumetric three-component and three-dimensional velocity measurements are performed for the axisymmetric turbulent pipe jet case. The dataset is validated extensively with a completely different and well-established measurement technique. A positive match between both techniques emphasizes the suitability of the V3V technique for measuring this type of flow field.

For leveraging the availability of a complete velocity gradient tensor, global entrainment in the spanwise plane of the jet is calculated and compared against the available literature. POD technique is applied for revealing the flow structure arrangements which govern the entrainment and ejection processes in a jet.

REFERENCES

Boersma, B. J., Brethouwer, G., and Nieuwstadt, F. T. M., 1998, "A Numerical Investigation on the Effect of the Inflow Conditions on the Self-Similar Region of a Round Jet", *Physics of Fluids*, Vol. 10, pp. 899–909.

Boomsma, A., and Troolin, D., 2018, "Time-Resolved Particle Image Identification and Reconstruction for Volumetric 4D-PTV", *Proceedings, 19th International Symposium on the Application of Laser and Imaging Techniques to Fluid Mechanics*, Lisbon, Portugal, July 16-19.

Breda, M., and Buxton, O. R. H., 2019, "Behaviour of Small-Scale Turbulence in the Turbulent/Non-Turbulent Interface Region of Developing Turbulent Jets", *Journal of Fluid Mechanics*, Vol. 879, pp. 187–216.

Capone, A., Soldati, A., and Romano, G. P., 2013, "Mixing and Entrainment in the Near Field of Turbulent Round Jets", *Experiments in Fluids*, Vol. 54, pp. 1434.

Cortina-Fernández, J., Sanmiguel Vila, C., Ianiro, A., and Discetti, S., 2021, "From Sparse Data to High-resolution Fields: Ensemble Particle Modes as a Basis for High-resolution Flow Characterization", *Experimental Thermal and Fluid Science*, Vol. 120, pp. 110178.

Crow, S. C., and Champagne, F. H., 1971, "Orderly Structure in Jet Turbulence", *Journal of Fluid Mechanics*, Vol. 48, pp. 547–591.

Discetti, S., and Coletti, F., 2018, "Volumetric Velocimetry for Fluid Flows", *Measurement Science and Technology*, Vol. 29, pp. 042001.

El Hassan, M., and Meslem, A., 2010, "Time-resolved Stereoscopic Particle Image Velocimetry Investigation of the Entrainment in the Near Field of Circular and Daisy-shaped Orifice Jets", *Physics of Fluids*, Vol. 22, pp. 035107.

Elsinga, G. E., Westerweel, J., Scarano, F., and Novara, M., 2011, "On the Velocity of Ghost Particles and the Bias Errors in Tomographic-PIV", *Experiments in Fluids*, Vol. 50, pp. 825–838.

Essel, E. E., Roussinova, V., and Balachandar, R., 2020, "Free Surface Effects on Spanwise Turbulent Structure in the Far-field of Submerged Jets", *Physics of Fluids*, Vol. 32, pp. 035108.

George, W. K., 1988, "Self-preservation, and Its Relation to Initial Conditions, and Coherent Structures", *Advances in Turbulence*, WK George & R Arndt, pp. 39–73.

Godbersen, P., and Schröder, A., 2020, "Functional Binning: Improving Convergence of Eulerian Statistics from Lagrangian Particle Tracking", *Measurement Science and Technology*, Vol. 31, pp. 095304.

Grinstein, F. F., 2001, "Vortex Dynamics and Entrainment in Rectangular Free Jets", *Journal of Fluid Mechanics*, Vol. 437, pp. 69–101.

Liepmann, D., and Gharib, M., 1992, "The Role of Streamwise Vorticity in the Near-field Entrainment of Round Jets", *Journal of Fluid Mechanics*, Vol. 245, pp. 643.

Meyer, K. E., Pedersen, J. M., and Özcan O., 2007, "A Turbulent Jet in Crossflow Analysed with Proper Orthogonal Decomposition", *Journal of Fluid Mechanics*, Vol. 583, pp. 199–227.

Romano, G., 2002, "The Effect of Boundary Conditions by the Side of the Nozzle of a Low Reynolds Number Jet", *Experiments in Fluids*, Vol. 33, pp. 323–333.

Sen, M., Bhaganagar, K., and Juttijudata, V., 2007, "Application of Proper Orthogonal Decomposition (POD) to Investigate a Turbulent Boundary Layer in a Channel with Rough Walls", *Journal of Turbulence*, Vol. 8, pp. N41.

Sirovich, L., 1987, "Turbulence and the Dynamics of Coherent Structures Part I: Coherent Structures", *Quarterly of Applied Mathematics*, Vol. 45, pp. 561–571.

Violato, D., and Scarano, F., 2011, "Three-dimensional Evolution of Flow Structures in Transitional Circular and Chevron Jets", *Physics of Fluids*, Vol. 23, pp. 124104.

Violato, D., and Scarano, F., 2013, "Three-dimensional Vortex Analysis and Aeroacoustic Source Characterization of Jet Core Breakdown", *Physics of Fluids*, Vol. 25, pp. 015112.

Wygnanski, I., and Fiedler, H., 1969, "Some Measurements in the Self-preserving Jet", *Journal of Fluid Mechanics*, Vol. 38, pp. 577–612.

Xu, G., and Antonia, R. A., 2002, "Effect of Different Initial Conditions on a Turbulent Round Free Jet", *Experiments in Fluids*, Vol. 33, pp. 677–683.

Zaman, K. B. M. Q., 1996, "Axis Switching and Spreading of an Asymmetric Jet: The Role of Coherent Structure Dynamics", *Journal of Fluid Mechanics*, Vol. 316, pp. 1–27.